In the format provided by the authors and unedited.

Pressure tuning of light-induced superconductivity in K$_3$C$_{60}$

A. Cantaluppi[1,2,6], M. Buzzi[1,6], G. Jotzu ![ORCID][1], D. Nicoletti[1,2], M. Mitrano ![ORCID][1], D. Pontiroli ![ORCID][3], M. Riccò[3], A. Perucchi[4], P. Di Pietro[4] and A. Cavalleri ![ORCID][1,2,5]*

[1]Max Planck Institute for the Structure and Dynamics of Matter, Hamburg, Germany. [2]The Hamburg Centre for Ultrafast Imaging, Hamburg, Germany. [3]Dipartimento di Scienze Matematiche, Fisiche e Informatiche, Università degli Studi di Parma, Parma, Italy. [4]INSTM UdR Trieste-ST and Elettra–Sincrotrone Trieste, Trieste, Italy. [5]Department of Physics, Oxford University, Clarendon Laboratory, Oxford, UK. [6]These authors contributed equally: A. Cantaluppi, M. Buzzi. *e-mail: andrea.cavalleri@mpsd.mpg.de

Supplementary Information

S1. Sample growth and characterisation.

Stoichiometric amounts of finely ground C_{60} powder and potassium metal were sealed in a cylindrical vessel and closed in a Pyrex vial under vacuum (~10^{-6} Torr). The potassium was kept separated from the fullerene powder during the thermal treatment, therefore only potassium vapors came in contact with C_{60}. The two reagents were heated at 523 K for 72 h and then at 623 K for 28 h. The vessel was then opened and the recovered black powder was reground and pelletized. Afterwards, the pellets were further annealed at 623 K for 5 days. All described operations were performed in inert atmosphere (vacuum or Ar glove box with <0.1 ppm O_2 and H_2O). The final product, K_3C_{60}, of an average grain size of 100-400 nm, was characterized by laboratory powder X-ray diffraction and SQUID magnetometry (Supplementary Fig. S1).
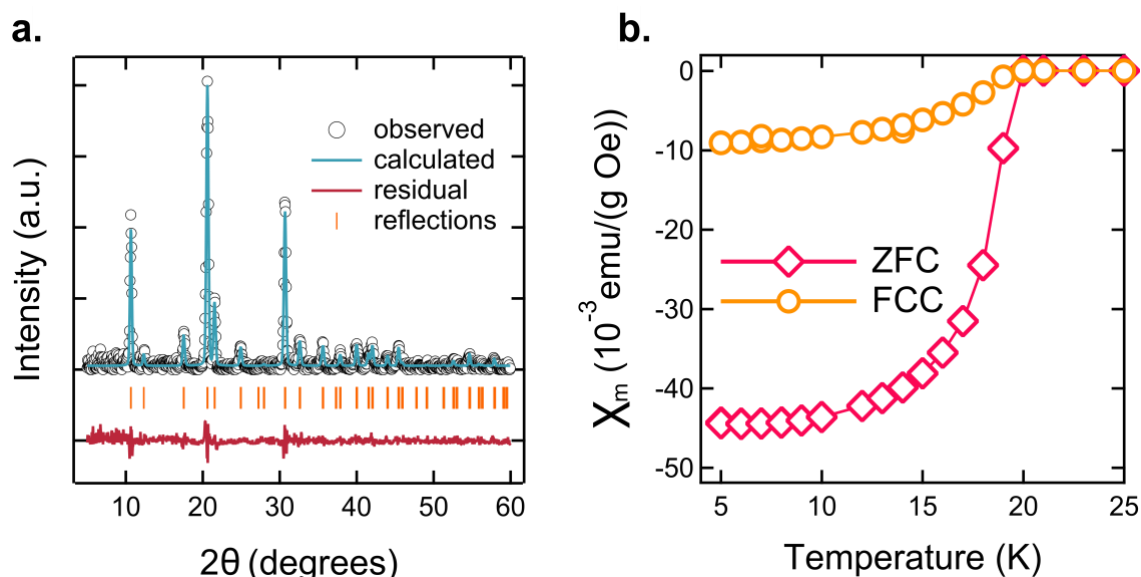
Supplementary Figure S1. K_3C_{60} sample characterisation. (**a**) Powder X-ray diffraction data for the K_3C_{60} used in this experiment together with a single f.c.c. phase Rietveld refinement. (**b**) Temperature dependence of the sample magnetic susceptibility with and without magnetic field (FCC: Field cooled cooling. ZFC: Zero field cooling).

S2. Equilibrium optical response under pressure.

The equilibrium optical properties of K_3C_{60} were determined in a broad spectral range (5 - 500 meV) for different temperatures and pressures. Fourier-transform infrared spectroscopy measurement were carried out at the SISSI beamline (Elettra Synchrotron Facility, Trieste), using a commercial Bruker Vertex70 interferometer equipped with an Hyperion microscope[1].

Hydrostatic pressure was applied by a screw-driven opposing plate diamond anvil cell (DAC) using Boehler-Almax type IIac diamond anvils with a culet size of 2 mm. K_3C_{60} powders (100 - 400 nm average grain size) were directly loaded in a 1 mm diameter sample compartment drilled in a 100 μm thick pre-indented Cu-gasket. This setup allowed achieving hydrostatic pressure values as high as 2.5 GPa, which were accurately measured *in situ* using a ruby fluorescence manometer[2,3]. The DAC was mounted on the cold finger of a liquid helium cryostat, which allowed varying the sample temperature. Note that all sample handling operations, including the loading of the K_3C_{60} powders in the DAC, were performed in an argon atmosphere glove box with < 0.1 ppm O_2 and H_2O in order to avoid oxygen contamination.

The equilibrium reflectivity of K_3C_{60} was measured at the sample-diamond interface by referencing against a gold mirror placed into the holder at the sample position. The experimental curves were then extrapolated at low frequency ($\lesssim$ 5 meV) using Drude-Lorentz fits, while for high frequencies ($\gtrsim$ 500 meV) literature data on K_3C_{60} single crystals[4] were used. We then performed a modified Kramers-Kronig transformation procedure for samples in contact with a transparent window[5], which allowed retrieving the complex optical conductivity of K_3C_{60} at all temperatures and pressures.

The response measured at ambient pressure was already reported in Ref. 6, where differences and analogies with data taken on single crystals[4] were also discussed. Here, in Supplementary Fig. S2, we show the equilibrium optical properties of K_3C_{60} measured for different pressures at a fixed temperature of T = 100 K.

All measured spectra have been consistently fitted using a Drude-Lorentz model, which included a free-carrier (*i.e.* Drude) term centered at $\omega = 0$ and a Lorentz oscillator at $\omega_{0,osc} \simeq$ 50 - 100 meV, which reproduced the mid-infrared absorption:

$$\sigma_1(\omega) + i\sigma_2(\omega) = \frac{\omega_p^2}{4\pi} \frac{1}{\gamma_D - i\omega} + \frac{\omega_{p,osc}^2}{4\pi} \frac{\omega}{i(\omega_{0,osc}^2 - \omega^2) + \gamma_{osc}\omega} \tag{1}$$

Here ω_p and γ_D are the Drude plasma frequency and scattering rate, while $\omega_{p,osc}^2$, γ_{osc}, and $\omega_{0,osc}$ stand for the oscillator strength, damping coefficient and resonant frequency of the Lorentz term.

In Supplementary Table S1 we report all parameters extracted from those fits. For each given temperature, we observe a monotonous increase in the low-frequency extrapolation of the real part of the optical conductivity, $\sigma_0 = \omega_p^2/(4\pi\gamma_D)$, with increasing hydrostatic pressure. This is the expected behavior for a conducting material in which the electronic bandwidth gets enhanced by compressing the crystal lattice. No defined trend is observed instead for the high-frequency absorption at $\omega \simeq$ 50 - 100 meV.

The equilibrium data reported here have been used, for each given temperature and pressure, to normalise the transient optical spectra of K_3C_{60} measured after photo-excitation, enabling the retrieval of all response functions of the perturbed material, as discussed in detail in the following sections.
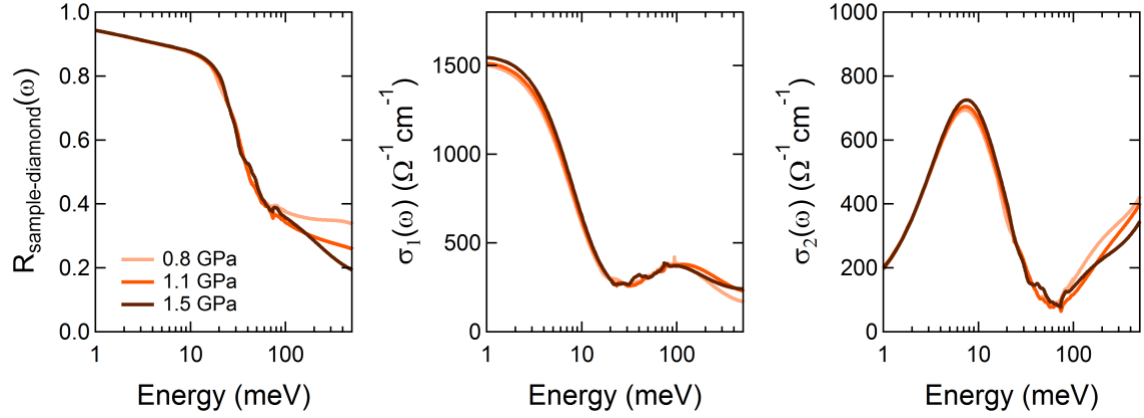
Supplementary Figure S2. Equilibrium optical properties of K₃C₆₀ under pressure. Equilibrium reflectivity at the sample-diamond interface (left), real (middle) and imaginary part (right) of the optical conductivity of K_3C_{60}, measured at T = 100 K for selected hydrostatic pressure values. Experimental data have been merged with extrapolations based on Drude-Lorentz fits below ~5 meV.

T(K)	P(GPa)	σ_0 ($\Omega^{-1}cm^{-1}$)	ω_p (meV)	γ_D (meV)	$\omega_{0,osc}$ (meV)	$\omega_{p,osc}$ (meV)	γ_{osc} (meV)
100	0.8 ± 0.1	1520 ± 20	300.2 ± 0.7	8.0 ± 0.1	76 ± 8	604.0 ± 0.6	160 ± 4
100	1.1 ± 0.1	1540 ± 20	307 ± 1	8.2 ± 0.1	80 ± 10	633 ± 1	190 ± 6
100	1.5 ± 0.1	1590 ± 30	313 ± 2	8.3 ± 0.1	70 ± 10	523 ± 2	165 ± 9
200	0.6 ± 0.1	1420 ± 20	295.0 ± 0.7	8.3 ± 0.1	75 ± 8	569.0 ± 0.7	154 ± 4
200	0.9 ± 0.1	1460 ± 30	308 ± 1	8.7 ± 0.1	81 ± 9	599.1 ± 0.9	155 ± 5
200	1.0 ± 0.1	1480 ± 20	300 ± 1	8.1 ± 0.1	67 ± 9	540 ± 1	150 ± 5
300	0.2 ± 0.1	1340 ± 20	290.8 ± 0.7	8.5 ± 0.1	70 ± 7	503.3 ± 0.6	141 ± 4
300	0.7 ± 0.1	1390 ± 40	300 ± 2	8.8 ± 0.2	86 ± 2	600 ± 20	200 ± 10
300	1.1 ± 0.1	1400 ± 20	298 ± 1	8.5 ± 0.1	66 ± 1	440 ± 9	135 ± 6

Supplementary Table S1. Drude-Lorentz fit parameters of the equilibrium data. Parameters extracted from Drude-Lorentz fits to the equilibrium optical response functions of K_3C_{60} measured at different temperatures and pressures. The parameters relative to the Drude term (plasma frequency ω_p, carrier scattering rate γ_D, and extracted zero-frequency conductivity σ_0) are displayed along with those of the mid-infrared absorption (center frequency $\omega_{0,osc}$, oscillator strength $\omega_{p,osc}$, and damping coefficient γ_{osc}). The pressure values were determined by fits of the ruby fluorescence line, as explained in Refs. 2,3.

S3. Time resolved THz spectroscopy under pressure

The transient optical response of K_3C_{60} after photo-excitation was measured under hydrostatic external pressure by means of time-resolved THz spectroscopy. Hydrostatic pressure was applied using a membrane-driven Diacell®Bragg-LT diamond anvil cell (DAC) from Almax easyLab, designed for cryogenic experiments. This DAC allowed varying the static pressure by actuating a membrane with helium gas, without removing the cell from its holder and ensuring maximum reliability and reproducibility of the measurement conditions. The DAC was mounted on the cold finger of a liquid helium cryostat, where the sample temperature was accurately measured using a ruby thermometer[3].

We used diamond anvils of type IIac with Boehler-Almax design and a culet size of 2 mm. K_3C_{60} powders (100 – 400 nm average grain size) were directly loaded in a 1.2 mm diameter sample compartment drilled in a 100 μm thick pre-indented Cu-gasket. Despite the relatively large sample compartment compared to the culet size of the anvils, no significant deformations were observed during the experiment. *In-situ* measurements of ruby R1 fluorescence line were used as a pressure gauge[2]. To avoid shifts in the pressure calibration axis due to different coupling of the fluorescence signal to the spectrometer, the fluorescence signal was passed through a single mode optical fiber. The overall accuracy of this measurement method is ~0.05 GPa. Pressure values as high as 2.5 GPa could be achieved. As in the case of the equilibrium characterisation (Supplementary Section S2), all sample handling operations were performed in an Ar atmosphere glove box with <0.1 ppm O_2 and H_2O in order to avoid oxygen contamination.

K_3C_{60} was excited using 300 fs long mid-infrared pulses with a spectrum centered at 7.3 μm wavelength (170 meV energy), tuned to resonance with an on-ball T_{1u} vibration. These pump pulses were generated by difference frequency mixing of the signal and idler outputs of a

two-stage optical parametric amplifier (OPA) in a 1 mm thick GaSe crystal. The OPA was pumped with 100 fs long pulses from a commercial Ti:Sapphire regenerative amplifier (800-nm wavelength). The pump pulses were then focused onto the sample, achieving a maximum fluence of ~3 mJ/cm^2, corresponding to peak electric fields of ~2.75 MV/cm.

The transient optical properties of K_3C_{60} after photo-excitation were measured using THz *probe* pulses with spectral bandwidth extending from 1 to 7.1 THz, *i.e.* 4.1 - 29 meV.

The probe pulses were generated and detected in 200-µm thick <110> GaP, using 35-fs-long 800-nm pulses. The time resolution of the pump probe experiment is of about 300 fs, as determined by the bandwidth of the THz-TDS setup[7,8] and by the mid-infrared pump pulse duration.

Note that, given the geometrical constraints of the experimental setup, only the frequency components of the probe spectrum above ~1.6 THz (6.5 meV) could be focused on a spot smaller than 1.2 mm, corresponding to the size of the compressed K_3C_{60} pellet. Therefore, unlike in the experiment of Ref. 6 (performed at ambient pressure and with a larger sample), here all frequencies smaller than the ~1.6 THz cut-off (6.5 meV) had to be excluded from our analysis, being most likely affected by spurious reflections from the highly reflective Cu-gasket surrounding the sample.

**S4. Measurement of the THz pump-induced changes under pressure**

The stationary electric field reflected by the sample, $E_R(t)$, and the pump-induced changes, $\Delta E_R(t,\tau) = E_R^{pumped}(t,\tau) - E_R(t)$, were simultaneously acquired at each time delay τ by filtering the electro-optic sampling signals with two lock-in amplifiers[9]. $\Delta E_R(t,\tau)$ and $E_R(t)$

were then independently Fourier transformed to obtain the complex-valued, frequency dependent $\Delta\tilde{E}_R(\omega,\tau)$ and $\tilde{E}_R(\omega)$.

The advantage of a double lock-in amplifier detection scheme relies on the simultaneous measurement of the light-induced changes and the reference electric field. This technique avoids the introduction of possible phase artifacts (e.g. due to long term drifts) and is particularly useful when the measured electric field contains fast-varying frequencies.

The raw pump-induced changes in reflected field amplitude, $\left|\Delta\tilde{E}_R(\omega,\tau)/\tilde{E}_R(\omega)\right|$, measured at T = 100 K and for a time delay $\tau = 1$ ps, are reported in Supplementary Fig. S3 for different applied pressures. Full spectra are shown on the left, while the pressure dependence of frequency-integrated values is displayed on the right.

Remarkably, the same trend found in the $\sigma_1(\omega)$ spectral weight loss in main text Fig. 4 (*i.e.* a reduction of the light-induced effect with increasing pressure), is also evident in the raw, unprocessed reflectivity changes reported here. This suggests that the main conclusion of our experiment, a reduction in the transient gap size with pressure, is clearly seen independent of any processing protocol.
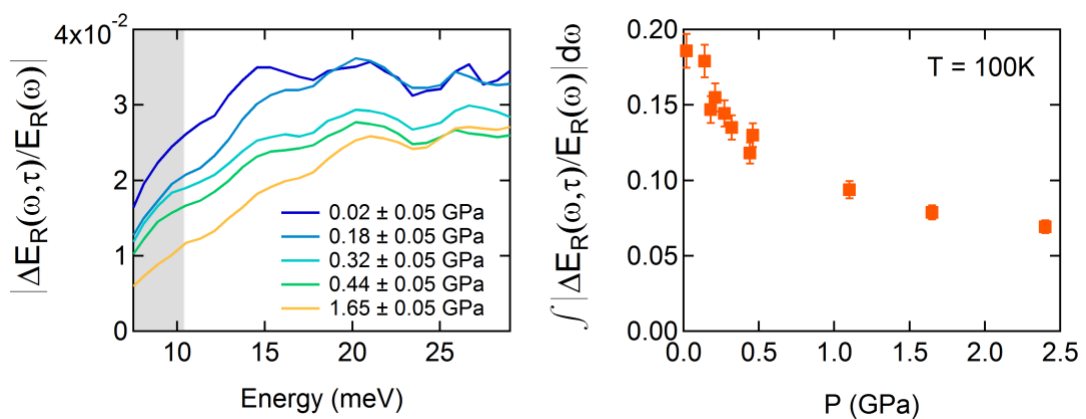
Supplementary Figure S3. Raw data analysis of K$_3$C$_{60}$ at 100K. (left panel) Evolution of the raw $\left|\frac{\Delta\tilde{E}_R(\omega,\tau)}{\tilde{E}_R(\omega)}\right|$ for selected values of external pressure, measured in K$_3$C$_{60}$ at 100K, at $\tau = 1$ ps after excitation. **(right panel)** Pressure dependence of the spectrally-integrated values. In analogy with main text Fig. 4, the integration was performed in the 6.5 − 12.9 meV range (gray shaded area in left panel).

S5. Determination of the transient optical properties.

The complex reflection coefficient of the photo-excited material, $\tilde{r}(\omega, \tau)$, was determined using the relation:

$$\frac{\tilde{r}(\omega, \tau) - \tilde{r}_0(\omega)}{\tilde{r}_0(\omega)} = \frac{\Delta\tilde{E}_R(\omega, \tau)}{\tilde{E}_R(\omega)} \qquad (2)$$

To calculate these ratios, the static reflection coefficient $\tilde{r}_0(\omega)$ was extracted at all temperatures and pressures from the equilibrium optical properties (see Supplementary Section S2).

These "raw" light-induced changes were then reprocessed to take into account the penetration depth mismatch between THz probe ($d_{probe} \simeq 0.6 - 0.9$ µm) and mid-infrared pump ($d_{pump} \simeq 0.2$ µm). A precise reconstruction method consists in treating the probed area of thickness $d_{probe}(\omega)$ as a stack of thin layers with a homogeneous refractive index and model the excitation profile as an exponential decay (see Supplementary Fig. S4). By calculating the coupled Fresnel equations of such multi-layer system, the complex refractive index at the surface, $\tilde{n}(\omega, \tau)$, can be self-consistently retrieved, and from this the complex conductivity for a volume that is homogeneously transformed,

$$\tilde{\sigma}(\omega, \tau) = \frac{\omega}{4\pi i}[\tilde{n}(\omega, \tau)^2 - \varepsilon_\infty]. \qquad (3)$$

Importantly, the only "free" parameter in our calculation is the penetration depth of the pump field, d_{pump}, the value of which is set by the equilibrium extinction coefficient at the pump wavelength, $Im(\tilde{n}_0(\omega = \omega_{pump}))$. On the other hand, the probe penetration depth, $d_{probe}(\omega, \tau)$, is a frequency and time-delay dependent quantity, which is extracted from the transient response of the material, $(Re(\tilde{n}(\omega, \tau)), Im(\tilde{n}(\omega, \tau)))$, obtained self-consistently through the multilayer model.

In order to minimize the effects of pump-probe time resolution due to a finite duration of the probe pulse, we operated the delay stages in the setup as explained in Ref. 7. Therefore, as already mentioned in Supplementary Section S3, our temporal resolution is limited only by the duration of the pump pulse and by the inverse bandwidth of the probe pulse. As discussed already in Ref. 6, for all measurements presented here the time resolution is of the order of 300 fs (see also Supplementary Section S3), the mid-infrared pump pulses are also ~300 fs long, transient coherence is induced in 1 ps, and the relaxation occurs within 2 − 10 ps. Therefore all possible spectral deformations are negligible[10,11].
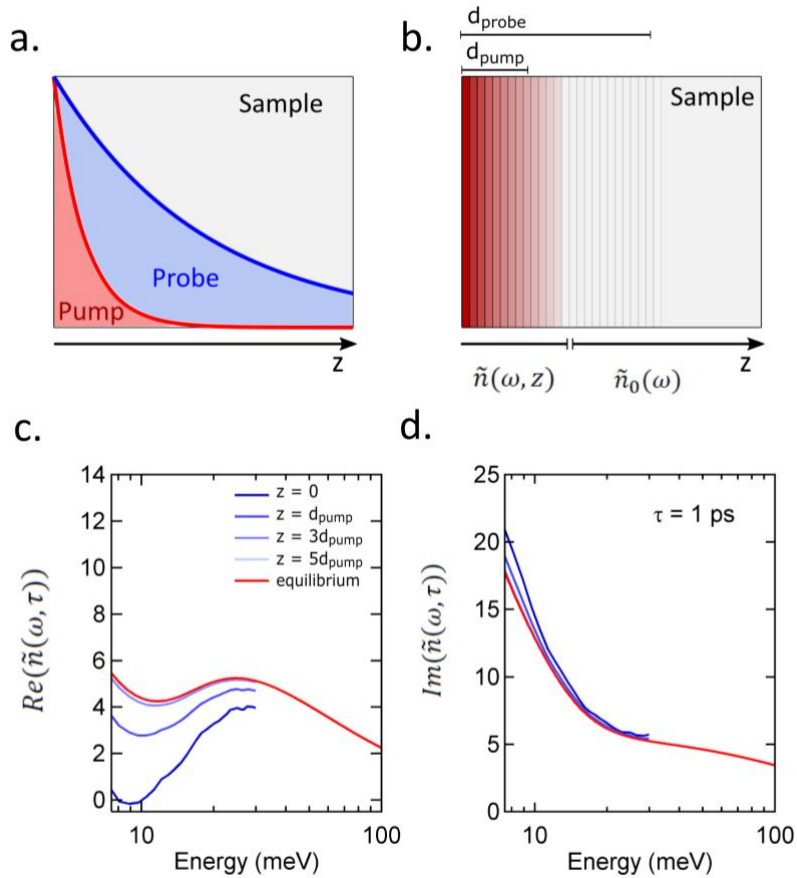

Supplementary Figure S4. Model for penetration depth mismatch. (**a**) Schematics of pump-probe penetration depth mismatch. (**b**) Multi-layer model with exponential decay used to calculate the pump-induced changes in the complex refractive index $\tilde{n}(\omega, \tau)$, for each pump-probe delay τ. The transition from red to background (grey) represents the decaying pump-induced changes in $\tilde{n}(\omega, \tau)$. (**c-d**) Depth-resolved changes in the real (**c**) and imaginary (**d**) part of the refractive index of K_3C_{60} (T = 100 K, P = 0 GPa), at τ = 1 ps pump-probe time delay. Spectra are displayed for different depths, ranging from z=0 (at the sample surface) to z=5d_{pump}. The equilibrium complex refractive index is shown in red.

S6. Influence of the choice of the penetration-depth mismatch model

As explained in Supplementary Section S5, the transient optical response functions reported in the main text have been reconstructed through a multi-layer model, in order to account for the pump-probe penetration depth mismatch. This model treats the excited sample as a stack of thin layers with a homogeneous refractive index, assuming an exponential excitation profile (see Supplementary Fig. S4). A valid, but less accurate alternative to such model can be obtained by considering the excited material as a single, uniform layer of thickness equal to the pump penetration depth, on top of an unperturbed bulk. As a benchmark, we extracted the transient optical properties using these two different models, starting from the "raw" light-induced changes measured at 1 ps pump–probe delay, T = 100 K, P = 0 GPa. Supplementary Fig. S5 shows the results of this comparison. The transient optical properties retrieved in the single-layer approximation (dark blue curves), and those obtained using a multi-layer model (light blue curves) only differ slightly. The qualitative features in the optical properties, e.g. the presence of a light-induced gap in the real part of the optical conductivity, are clearly independent on the model chosen to account for the penetration depth mismatch.
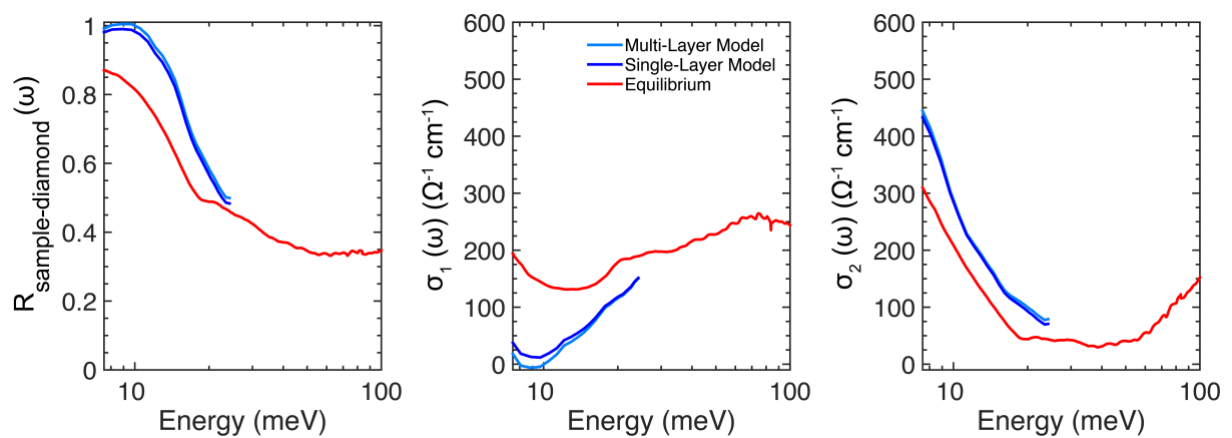
Supplementary Figure S5. Multi-layer model vs Single-layer model. Reflectivity, R(ω), and complex optical conductivity, σ(ω), of K_3C_{60} measured at τ = 1 ps pump–probe delay, T = 100 K, P = 0 GPa. Light-blue curves are obtained using the single-layer model; dark-blue curves are retrieved using the multi-layer model.

S7. Influence of uncertainties in the equilibrium optical properties

The error on the reconstructed transient optical response of photo-excited K_3C_{60} are primarily determined by (i) the uncertainty in the absolute value of the measured equilibrium reflectivity, which is typically of the order of ±1%, and (ii) by the value of the pump penetration depth d_{pump} used to reconstruct the $\tilde{n}(\omega, z)$ profile in the multilayer model. Similar to Supplementary Section S6, we use as benchmark the transient optical properties reconstructed from the recorded "raw" light-induced changes measured at 1 ps pump–probe delay, T = 100 K, P = 0 GPa.
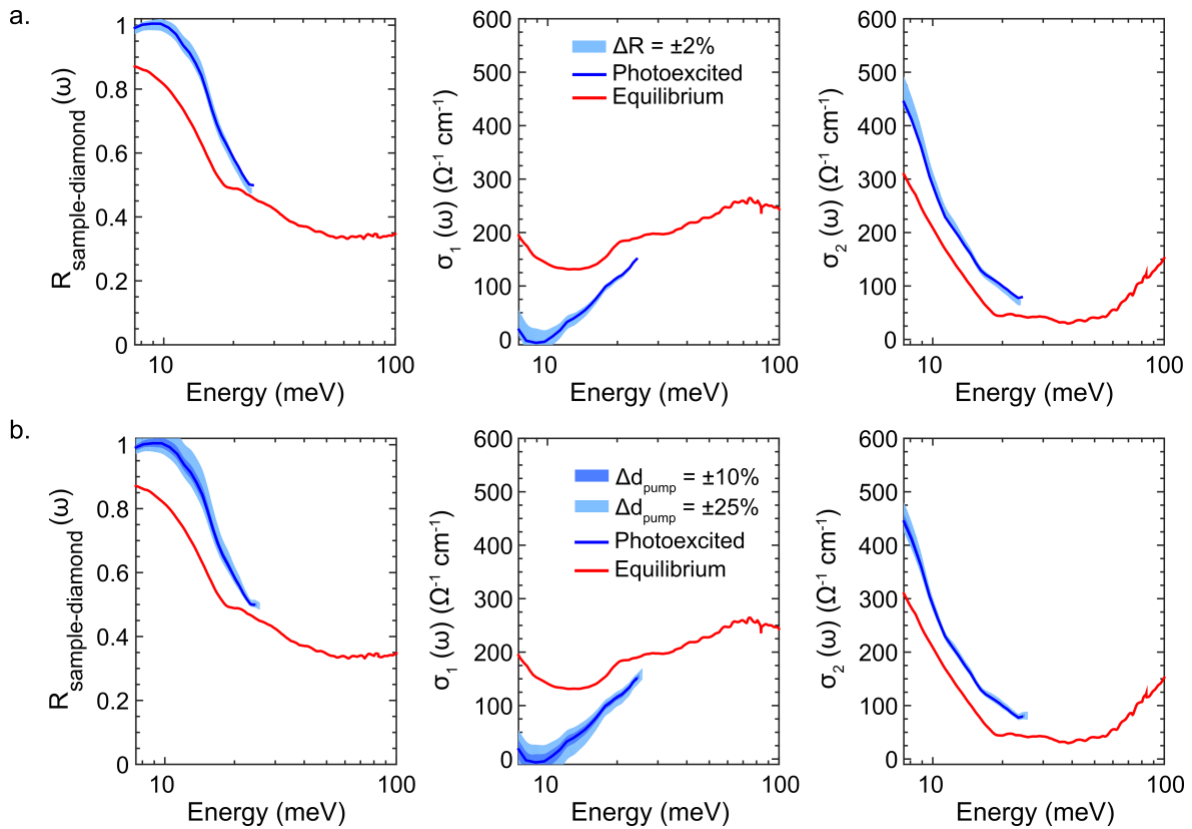

Supplementary Figure S6. Error in the retrieved transient optical properties originated by uncertainties in the equilibrium optical properties. Red and dark-blue curves are the T = 100 K, P = 0 GPa reflectivity and complex optical conductivity of K_3C_{60} measured at equilibrium and at τ = 1 ps pump–probe time delay, respectively. Error bars, shown as colored bands, have been propagated from **(a)** a ±2% uncertainty in the value of the equilibrium R(ω), **(b)** a ±10% (dark-blue shading) and ±25% (light-blue shading) uncertainty in the value of the pump penetration depth.

Supplementary Fig. S6a and S6b show as colored bands the propagated error bars in the transient optical properties for maximum uncertainties of ±2% in the equilibrium R(ω) and of ±10% and ±25% in d_{pump}, respectively. Importantly, all qualitative features in the retrieved response of the perturbed material, as for example the presence of a light-induced gap in the real part of the optical conductivity, remain unaffected.

## S8. Time evolution of the transient optical response of K_3C_{60} under pressure

The temporal evolution of the light-induced state in K_3C_{60} does not show a strong pressure dependence and resembles that observed under ambient conditions[6]. Supplementary Fig. S7 shows the frequency averaged "raw" reflectivity changes as function of pump-probe time delay for selected values of external pressure. Those curves have been obtained by sampling the peak of the THz-probe electric field at different time delays before and after excitation.
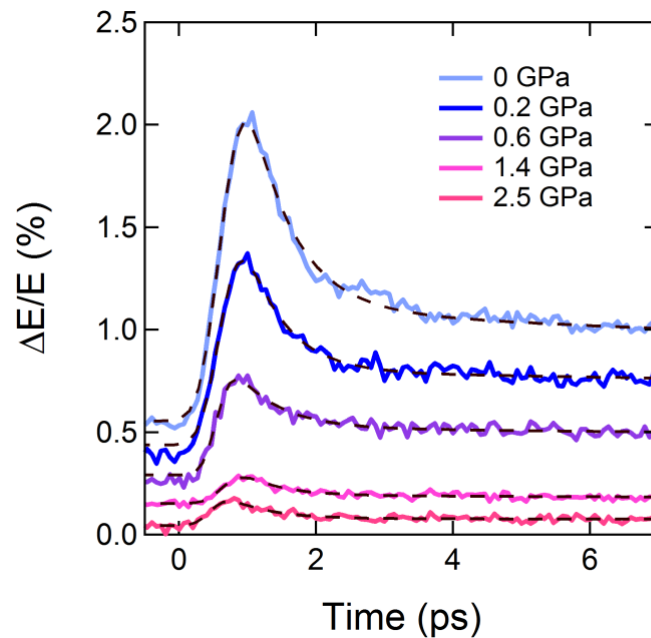
Supplementary Figure S7. Time evolution of the photo-excited state in K_3C_{60} under pressure. Frequency averaged changes in the reflected THz field as function of time delay, for selected values of external pressure, measured at T = 100 K. The experimental data (solid lines) have been obtained by sampling the peak of the THz-probe electric field as a function of pump-probe delay. Dashed lines are exponential fits. Rigid vertical offsets have been introduced for clarity.

Independent of the specific value of the external pressure, the light-induced reflectivity changes are always positive (see also Fig. 3 of the main text). All curves in Supplementary Fig. S7 have been fitted with a double exponential decay with relaxation time constants $\tau_1 \sim 1$ ps and $\tau_2 \gg 10$ ps.

Supplementary Fig. S8 shows the transient optical properties of K_3C_{60} measured at T = 300 K and P = 0.03 GPa for four representative pump-probe delays. The light-induced changes in the optical properties are largest at early times (τ = 0.8, 1 ps) and become progressively smaller at later delays (τ = 2 ps). Similar data have already been reported for K_3C_{60} at ambient pressure in Ref. 6.
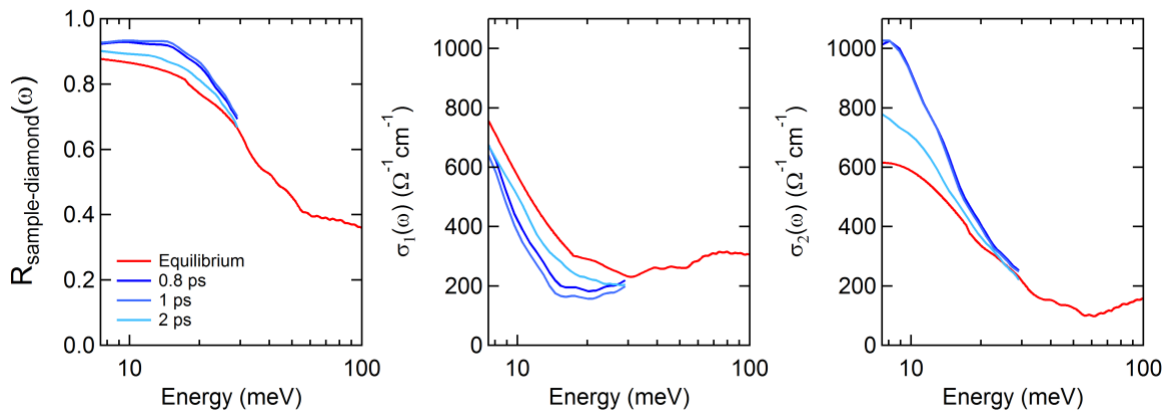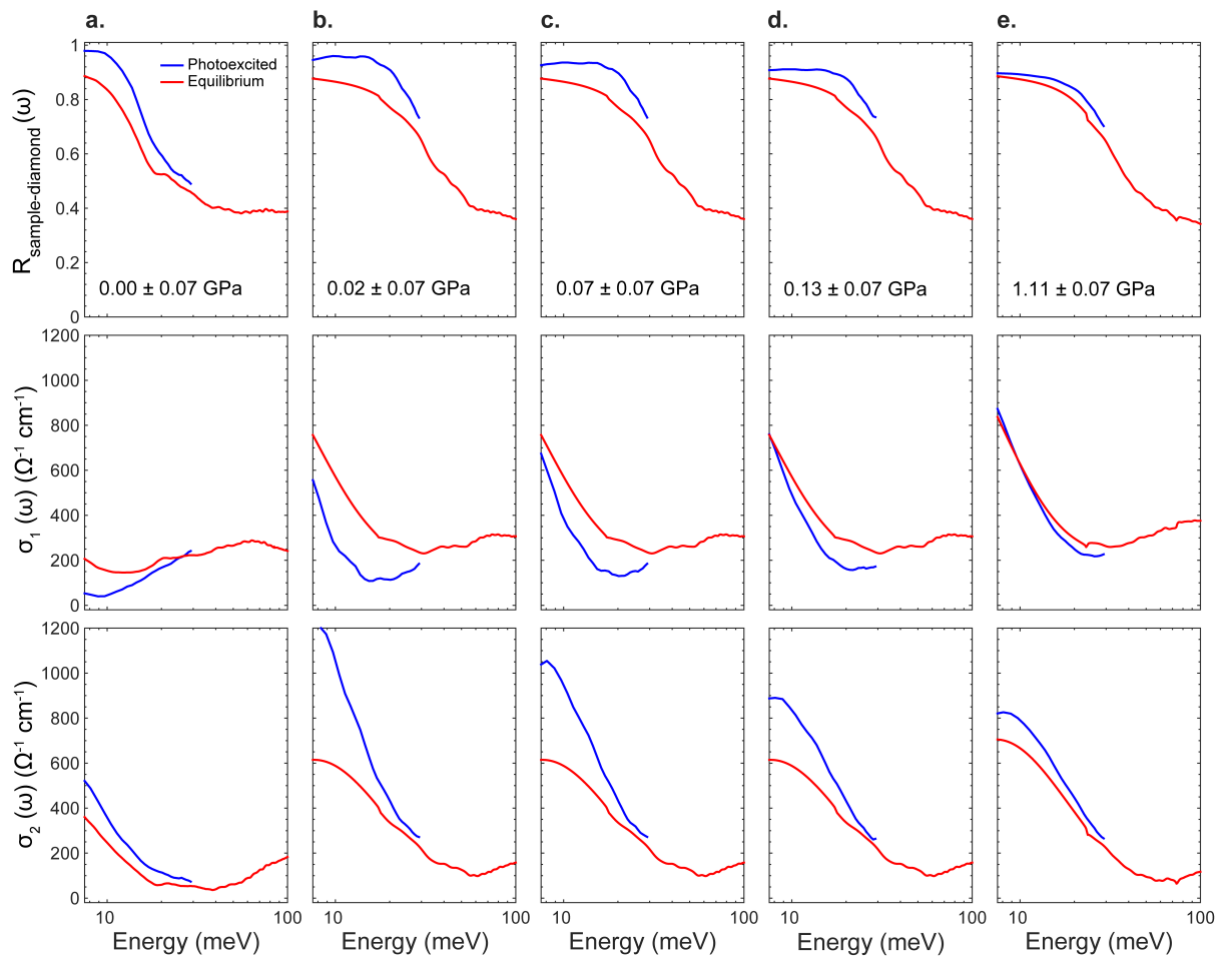

Supplementary Figure S8. Transient optical properties of K_3C_{60} at different pump-probe delays. Reflectivity at the sample-diamond interface (left), real (middle) and imaginary part (right) of the optical conductivity of K_3C_{60}, measured at T = 300 K and P = 0.03 ± 0.05 GPa for selected pump-probe delays. All data were taken with the same pump fluence (3 mJ/cm^2).
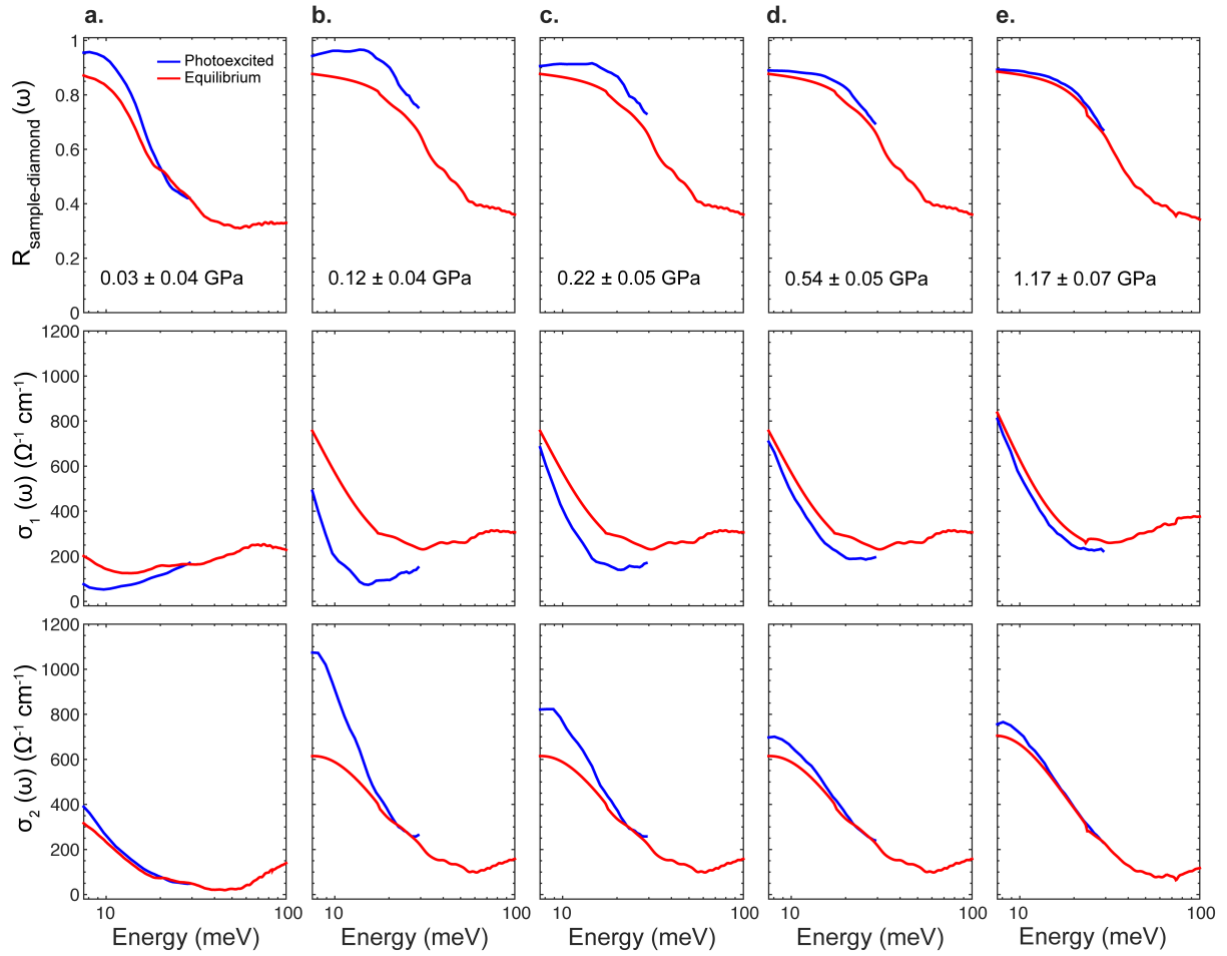
S9. Pressure-dependent transient optical properties at T = 200 K and T = 300 K.

The pressure dependence of the transient optical properties of K_3C_{60}, measured at τ = 1 ps and T = 100 K, is displayed in Fig. 3 of the main text. Supplementary Fig. S9 and S10 show additional data set measured at higher temperatures, T = 200 K and T = 300 K, respectively.

For both temperatures, the ambient pressure response shows a partial light-induced gapping in $\sigma_1(\omega)$, accompanied by a low-frequency divergence in $\sigma_2(\omega)$. On the other hand, at higher pressures, the photo-induced changes are gradually suppressed and the measured transient conductivity evolves into that of a metal with enhanced carrier mobility (narrower Drude peak).

Supplementary Figure S9. Pressure dependence of the transient optical properties of K$_3$C$_{60}$ at T = 200 K. Reflectivity at the sample-diamond interface and complex optical conductivity of K$_3$C$_{60}$ measured at equilibrium (red) and 1 ps after photoexcitation (blue) at T = 200 K, for different external hydrostatic pressures. All data were taken with the same pump fluence (3 mJ/cm^2).

Supplementary Figure S10. Pressure dependence of the transient optical properties of K₃C₆₀ at T = 300 K. Reflectivity at the sample-diamond interface and complex optical conductivity of K_3C_{60} measured at equilibrium (red) and 1 ps after photoexcitation (blue) at T = 300 K, for different external hydrostatic pressures. All data were taken with the same pump fluence (3mJ/cm^2).

As discussed in the main text, in this high temperature regime, a high-mobility metallic state was proposed in Ref. 6 to interpret the ambient pressure data. However, this interpretation was also not unique, as a superconducting-like state with progressively lower coherence would have also been consistent with the measured spectra. Figure 5b-c of the main text, whose data points have been extracted from fits to the data of Supplementary Fig. S9 and S10, clearly shows that in the low-pressure regime a decreasing zero-frequency conductivity, σ_0, with increasing pressure is retained all the way to T = 300 K, suggesting that some

incipient features of a transient superconducting state may already be present up to room temperature.

S10. Drude-Lorentz fits of the out-of-equilibrium optical response

The transient optical properties of K_3C_{60} were modeled at all measured temperatures and pressures by fitting the perturbed reflectivity and complex optical conductivity simultaneously, using the same Drude-Lorentz model which was employed to fit the equilibrium response (see Supplementary Section S2):

$$\sigma_1(\omega) + i\sigma_2(\omega) = \frac{\omega_p^2}{4\pi}\frac{1}{\gamma_D - i\omega} + \frac{\omega_{p,osc}^2}{4\pi}\frac{\omega}{i(\omega_{0,osc}^2 - \omega^2) + \gamma_{osc}\omega} \tag{4}$$

This model is obviously expected to fully capture the metallic character of the transient optical properties measured at high pressure. In addition, while more accurate modelling has been used in Ref. 6 to describe the transient superconducting-like response of K_3C_{60}, it is worth noting that even the simple $\gamma_D \to 0$ limit of the Drude conductivity used here can capture the response of a superconductor below gap:

$$\sigma_1(\omega) + i\sigma_2(\omega) = \frac{\pi}{2}\frac{N_S e^2}{m}\delta[\omega = 0] + i\frac{N_S e^2}{m}\frac{1}{\omega}. \tag{5}$$

Here N_S, e, and m are the superfluid density, electron charge, and electron mass, respectively. Importantly, the transient nature of a superconductor with finite lifetime appears in the above formula as a broadening in the linewidth of the zero-frequency Dirac delta[12].

In Supplementary Fig. S11 we report two representative fits to 100 K data measured at ambient pressure and at 0.26 ± 0.05 GPa, which all show a good agreement with the experiment. Both transient data sets (blue curves) could be fitted with the Drude model described in Eq. 4 using as initial guess the fit parameters of the corresponding equilibrium

data sets (red curves). Fits were performed by either keeping the high-frequency (> 40 meV) mid-infrared oscillator fixed (grey dashed line), or by letting it evolve freely (black dash-dotted line). Remarkably, both fits returned very similar results, with identical Drude parameters within the error bars. We therefore chose to rely on the model with the least number of free parameters (gray dashed lines).

In Supplementary Table S2 we show the Drude parameters for all data sets (extracted from the fits with fixed mid-infrared absorption band). Note that the calculated zero-frequency extrapolations of the optical conductivity, σ_0, reported in this table are also plotted and discussed in the main text (see Fig. 5).
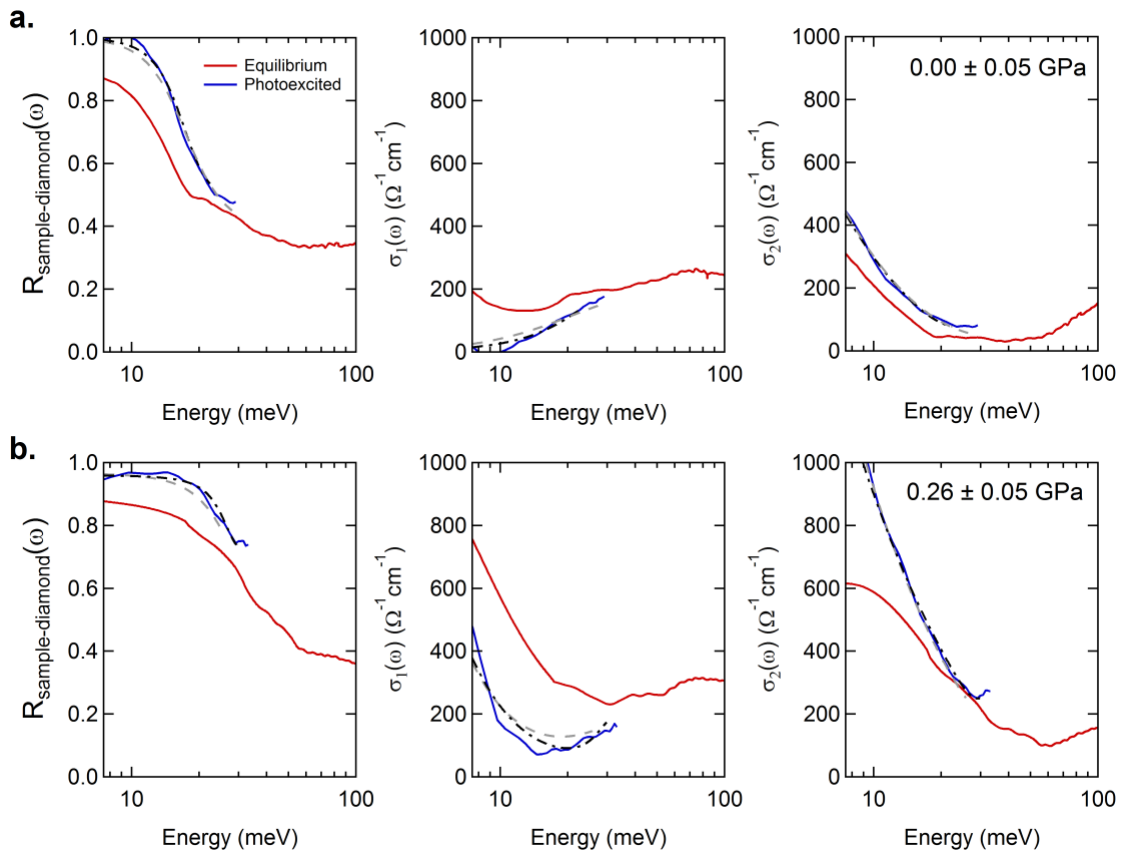
Supplementary Figure S11. Drude-Lorentz fits to the transient optical response. Reflectivity at the sample-diamond interface and complex optical conductivity of K_3C_{60} measured at equilibrium (red) and 1 ps after photoexcitation (blue) for T = 100 K at ambient pressure (**a**) and at P = 0.26 ± 0.05 GPa (**b**). Experimental data (full lines) are displayed along with Drude-Lorentz fits, performed by either keeping the high-frequency (> 40 meV) mid-infrared oscillator fixed (grey dashed line), or by letting it evolve freely (black dash-dotted line).

T(K)	P(GPa)	σ_0 (Ω^{-1}cm^{-1})	ω_P (meV)	γ_D (meV)
100	0.02 ± 0.05	$10^{17} \pm 10^{13}$	169 ± 3	0.0 ± 0.3
100	0.05 ± 0.05	$10^{18} \pm 10^{12}$	280 ± 4	0.0 ± 0.3
100	0.14 ± 0.05	17000 ± 8000	279 ± 4	0.6 ± 0.3
100	0.18 ± 0.05	7000 ± 1000	276 ± 3	1.4 ± 0.3
100	0.21 ± 0.05	8000 ± 1000	276 ± 3	1.3 ± 0.2
100	0.27 ± 0.05	6200 ± 800	277 ± 3	1.7 ± 0.2
100	0.32 ± 0.05	5100 ± 500	278 ± 3	2.0 ± 0.2
100	0.44 ± 0.05	4800 ± 600	263 ±3	2.0 ± 0.3
100	0.46 ± 0.05	3900 ± 300	281 ±6	2.7 ± 0.2
100	1.10 ± 0.05	3900 ± 400	284 ± 3	2.8 ± 0.3
100	1.70 ± 0.06	3100 ± 300	294 ± 4	3.7 ± 0.3
100	2.40 ± 0.09	3700 ± 300	310 ± 4	3.5 ± 0.3
200	0.00 ± 0.07	$10^{18} \pm 10^{12}$	191 ± 1	0.0 ± 0.1
200	0.02 ± 0.06	4500 ± 300	293 ± 2	2.5 ± 0.2
200	0.07 ± 0.07	3000 ± 200	293 ± 2	3.8 ± 0.2
200	0.13 ± 0.07	2100 ± 100	293 ± 2	5.1 ± 0.2
200	0.22 ± 0.07	2020 ± 80	295 ± 2	5.8 ± 0.2
200	0.41 ± 0.07	1790 ± 50	298 ± 2	6.7 ± 0.2
200	1.10 ± 0.07	1920 ± 40	310 ± 2	6.7 ± 0.1
300	0.03 ± 0.04	4700 ± 800	169 ± 1	0.8 ± 0.1
300	0.03 ± 0.04	2700 ± 100	280 ± 2	3.8 ± 0.2
300	0.07 ± 0.04	4900 ± 400	275 ± 2	2.0 ± 0.2
300	0.12 ± 0.04	4500 ± 400	275 ± 3	2.3 ± 0.2
300	0.23 ± 0.05	2200 ± 100	277 ± 3	4.7 ± 0.2
300	0.54 ± 0.05	1660 ± 50	279 ± 2	6.3 ± 0.2
300	1.17 ± 0.07	1750 ± 30	297 ± 1	6.8 ± 0.1

Supplementary Table S2. Drude parameters extracted from fits to the transient data. Parameters extracted from Drude-Lorentz fits to the transient optical response functions of K_3C_{60} measured at different temperatures and pressures. The plasma frequency ω_P, Drude scattering rate γ_D, and extracted dc conductivity σ_0 are displayed. The pressure values are extracted by fits of the ruby fluorescence line, as explained in Refs. 2,3.

REFERENCES (Supplementary Information)

1. Lupi, S. *et al.* Performance of SISSI, the infrared beamline of the ELETTRA storage ring. *J. Opt. Soc. Am. B* **24,** 959 (2007).

2. Mao, H. K., Xu, J. & Bell, P. M. Calibration of the ruby pressure gauge to 800 kbar under quasi-hydrostatic conditions. *J. Geophys. Res.* **91,** 4673 (1986).

3. Weinstein, B. A. Ruby thermometer for cryobaric diamond-anvil cell. *Rev. Sci. Instrum.* **57,** 910–913 (1986).

4. Degiorgi, L., Briceno, G., Fuhrer, M. S., Zettl, A. & Wachter, P. Optical measurements of the superconducting gap in single-crystal K_3C_{60} and Rb_3C_{60}. *Nature* **369,** 541–543 (1994).

5. Plaskett, J. S. & Schatz, P. N. On the Robinson and Price (Kramers-Kronig) Method of Interpreting Reflection Data Taken through a Transparent Window. *J. Chem. Phys. Vol.* **38,** 612–617 (1963).

6. Mitrano, M. *et al.* Possible light-induced superconductivity in K_3C_{60} at high temperature. *Nature* **530,** 461–464 (2016).

7. Kindt, J. T. & Schmuttenmaer, C. A. Theory for determination of the low-frequency time-dependent response function in liquids using time-resolved terahertz pulse spectroscopy. *J. Chem. Phys.* **110,** 8589–8596 (1999).

8. Schmuttenmaer, C. A. Exploring dynamics in the far-infrared with terahertz spectroscopy. *Chem. Rev.* **104,** 1759–1779 (2004).

9. D'Angelo, F. *et al.* Self-referenced ultra-broadband transient terahertz spectroscopy using air-photonics. *Opt. Express* **24,** 10157 (2016).

10. Nicoletti, D., Mitrano, M., Cantaluppi, A. & Cavalleri, A. Comment on 'Terahertz time-domain spectroscopy of transient metallic and superconducting states (arXiv:1506.06758) '. *arXiv:1506.07846* (2015).

11. Kennes, D. M., Wilner, E. Y., Reichman, D. R. & Millis, A. J. Nonequilibrium optical conductivity: General theory and application to transient phases. *Phys. Rev. B* **96,** 54506 (2017).

12. Nicoletti, D. *et al.* Optically induced superconductivity in striped $La_{2-x}Ba_xCuO_4$ by polarization-selective excitation in the near infrared. *Phys. Rev. B* **90,** 100503(R) (2014).